PROCEEDINGS OF SCIENCE

PoS(ICRC2023)018

The latest time variation measurements with AMS

Miguel Angel Velasco[a,*] **for the AMS collaboration**

[a] *Centro de Investigaciones Energéticas, Medioambientales y Tecnológicas (CIEMAT),*
Avda. Complutense 40, Madrid, Spain

E-mail: miguelangel.velasco@ciemat.es

Charged cosmic rays entering the solar system are affected by the interaction with the expanding turbulent solar wind and the interplanetary magnetic field. This process, known as solar modulation, introduces a time variation in the cosmic ray fluxes measured near Earth for rigidities up to a few tens of GV. In twelve years of operation, AMS has measured the temporal structures of fluxes of elementary particles and light nuclei up to Oxygen over an eleven-year solar cycle. The detailed time dependence measurements of these fluxes reveal variations on different time scales and rigidities associated to the solar activity. This extensive set of continuous measurements performed by a single detector over a long time period provides valuable information about both the mass and charge sign dependencies of the solar modulation of cosmic rays.

Thanks to its large acceptance, identification capabilities and long-term mission in space, AMS is a unique experiment to carry out precise studies on the time variability of the individual species in cosmic rays. These results provide fresh insights for an in-depth understanding of cosmic rays in the heliosphere.

38th International Cosmic Ray Conference (ICRC2023)
26 July - 3 August, 2023
Nagoya, Japan

ICRC2023
38th International Cosmic Ray Conference
The Astroparticle Physics Conference

---

[*] Speaker

1. Introduction

The fluxes of charged cosmic rays outside the heliosphere are thought to be stable on the timescale of decades [1–4]. Time-dependent variations in the fluxes of galactic cosmic rays measured inside the heliosphere are only expected from the solar modulation [5]. These variations correlate with solar activity at different timescales [5, 6]. The most significant long-term scale variation is the 11-year solar cycle during which the number of sunspots changes from minimum to maximum and then back to a minimum [7, 8]. Shorter scale variations can be either nonrecurrent or recurrent. The nonrecurrent variations are mainly due to the interactions of cosmic rays with strong transient disturbances in the interplanetary magnetic field, such as shock waves generated by interplanetary coronal mass ejections, especially during solar maxima, that can last from days to weeks [9]. Recurrent variations with a period of 27 days, corresponding to the synodic solar rotation, and at multiples of that frequency (e.g., periods of 13.5 and 9 days) are related to the passage of corotating interaction regions originating from one or more coronal holes of the Sun [10–18], as first observed in 1938 [19]. Previous studies on the estimated rigidity[1] dependence in periodicities, for example in [15], generally concluded that the power of the periodicity decreases with increasing rigidity. This formed the paradigm over the AMS rigidity range (1 to 100 GV) that the strength of the 27-day (and 13.5-day, 9-day) periodicities steadily decreases with increasing rigidity of cosmic rays, differently in solar maximum and minimum [20]. However, recent AMS results on periodicities in proton, helium and electron daily fluxes [21–23] do not support that the strength of the periodicities would always decrease with increasing rigidity.

Solar modulation involves convective, diffusive, particle drift, and adiabatic energy loss processes [6]. Only particle drift induces a dependence of solar modulation on the particle charge sign [24]. According to models based on the Parker equation [6], the time dependence of distinct nuclei fluxes (p, He, etc.) evaluated at the same rigidity might differ because of (a) differences in the flux rigidity dependence outside the heliosphere, (b) differences in velocity because of distinct mass-to-charge ratio [25], and (c) solar wind turbulence and other interplanetary parameters. Since positrons and electrons differ only in charge sign, positrons and protons share the same charge sign with different masses, and helium provides different information on both charge and mass, their simultaneous measurement over an eleven-year solar cycle offers a unique way to study charge-sign and mass dependent solar modulation effects at different time scales.

2. AMS detector

The Alpha Magnetic Spectrometer (AMS) experiment is a magnetic spectrometer onboard the International Space Station (ISS) devised to provide precision measurements of charged cosmic rays up to $Z = 28$ and energies up to few TeV. AMS has been designed and built by an international collaboration that includes institutes from Europe, Asia and America. It was installed on May 19, 2011 onboard the ISS and it continues taking data steadily since then. So far, AMS has collected more than 220 billion events of galactic cosmic rays in a long-term mission spanning the ISS lifetime, currently until 2030.

---

[1] Momentum per unit of charge, $R = p/Z$.

The layout of the AMS detector is shown in Fig. 1. The core of the detector is a permanent magnet hosting 7 layers of silicon detectors (Tracker) that provide a measurement of the momentum, charge and charge sign from the curvature of the trajectory of the incoming particle. Two additional silicon layers are located at the top and bottom of the detector to increase the lever arm in the measurement of the trajectory of high-energy particles. A time-of-flight (TOF) system, made of of two double layers of scintillators, is located above and below the magnet. The TOF delivers the main trigger to the detector and provides a measurement of the velocity and charge of the particles. A transition radiation detector (TRD) is located on top of the Upper-TOF and allows for the separation of light and heavy particles. In particular, it provides identification capabilities to distinguish electrons and positrons from protons. Below the Lower-TOF, a Ring Imaging Cherenkov Detector (RICH) measures accurately the velocity of the traversing charged particle allowing for isotopic identification. At the bottom of AMS, an electromagnetic calorimeter (ECAL) measures the energy of electromagnetic showers up to TeV energies. The ECAL is a fine granularity 3D calorimeter able to reconstruct the shape of the showers, thus providing additional information for the electron and positron identification. An array of 16 anti-coincidence counters (ACC) surrounds the Tracker detector inside the magnet bore. Their purpose is to reject particles that enter or exit the tracker volume transversely. A detailed description of the detector and its performances can be found in [26].

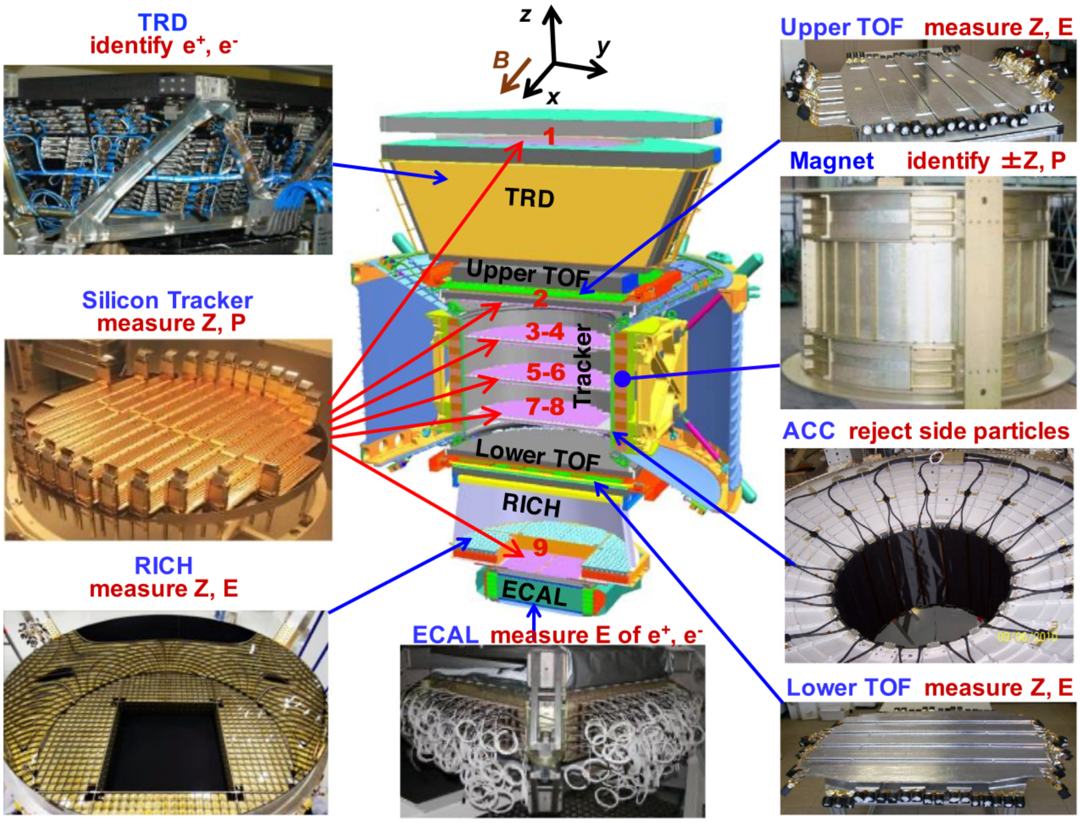

Figure 1: AMS Detector showing the main elements and their functions. The AMS coordinate system, concentric with the magnet, is also shown. The X axis is parallel to the main component of the magnetic field and the Z axis is pointing vertically.

Due to its capability to perform precision and redundant measurements of the properties of the particles, excellent particle identification including matter-antimatter separation, large acceptance and long-duration data taking in space, AMS is a unique experiment to perform accurate measurements of elementary particles, nuclei and anti-nuclei in the cosmic rays.

3. Periodicities in the Daily Proton Fluxes

We present the daily time evolution of the proton flux from 1.00 to 100 GV. The measurement is based on 6.3×10^9 protons collected by AMS during the first 10.5 years of operation. These data cover the major portion of solar cycle 24, which includes the polarity reversal of the solar magnetic field in the year 2013 [27], and the beginning of solar cycle 25. This is an update of the published AMS daily proton fluxes based on the first 8.5 years of operation in [21]. See also [28] for more details.

Fig. 2(a) shows the daily proton fluxes, Φ_p, for six rigidity bins from 1.00 to 10.10 GV measured from May 20, 2011 to November 2, 2021. As seen, the proton fluxes exhibit variations on different time scales, from days to years. The relative magnitude of these variations decreases with increasing rigidity. At low rigidities, recurrent flux variations are clearly visible. Fig. 2(b) shows the daily AMS proton fluxes measured in 2016 for three rigidity bins [1.00–1.16] GV, [5.90–6.47] GV, and [16.60–22.80] GV. As seen, double-peak and triple-peak structures are visible in different Bartels rotations (BR: 27 days).

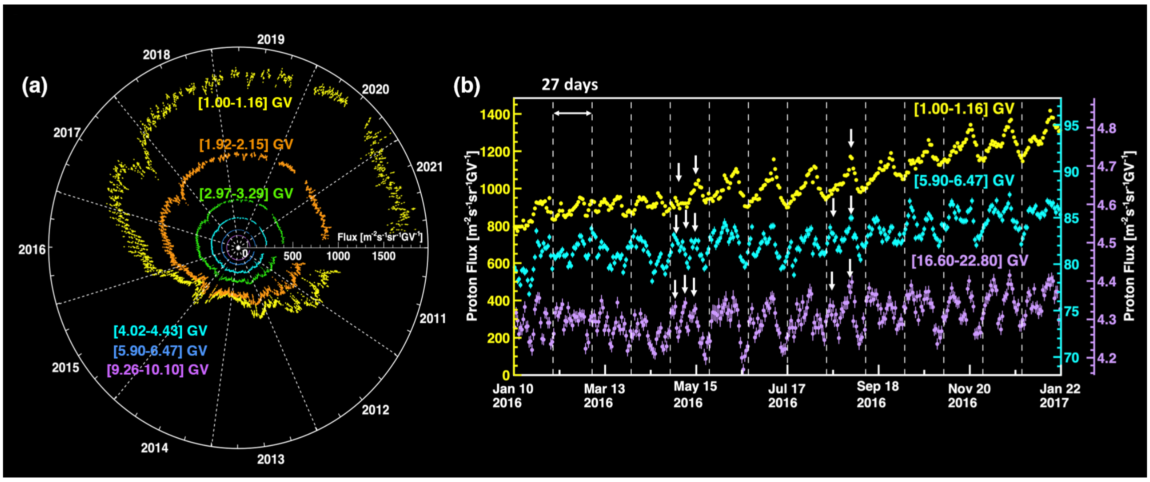

Figure 2: (a) The daily AMS proton fluxes, Φ_p, in units of $[\mathrm{m}^{-2}\mathrm{sr}^{-1}\mathrm{s}^{-1}\mathrm{GV}^{-1}]$ for six rigidity bins from 1.00 to 10.10 GV measured from May 20, 2011 to November 2, 2021. (b) The daily proton fluxes measured in 2016 for three rigidity bins. Vertical dashed lines separate Bartels rotations. As seen, double-peak and triple-peak structures are visible in different Bartels rotations.

To study the recurrent time variations in the daily proton fluxes, a wavelet time-frequency technique [29] was used to locate the time intervals where the periodic structures emerge. We observed recurrent flux variations with a period of ~ 27 days with significance above the 95% confidence level from 2014 to 2018. Shorter periods of ~ 13.5 days and ~ 9 days are significant only in 2016.

Fig. 3 shows the normalized power as a function of rigidity and period for the for the first and the second half of 2016. The normalized power is defined by the power divided by the variance of the time series and indicates the strength of the periodicity. As seen, the strength of all three periodicities is rigidity dependent. In particular, the strength of 9-day and 13.5-day periodicities increases with increasing rigidity up to ∼ 10 GV and ∼ 20 GV, respectively, and then decreases with increasing rigidity up to 100 GV. Thus, the AMS results do not support the general conclusion that the strength of the periodicities steadily decreases with increasing rigidity.

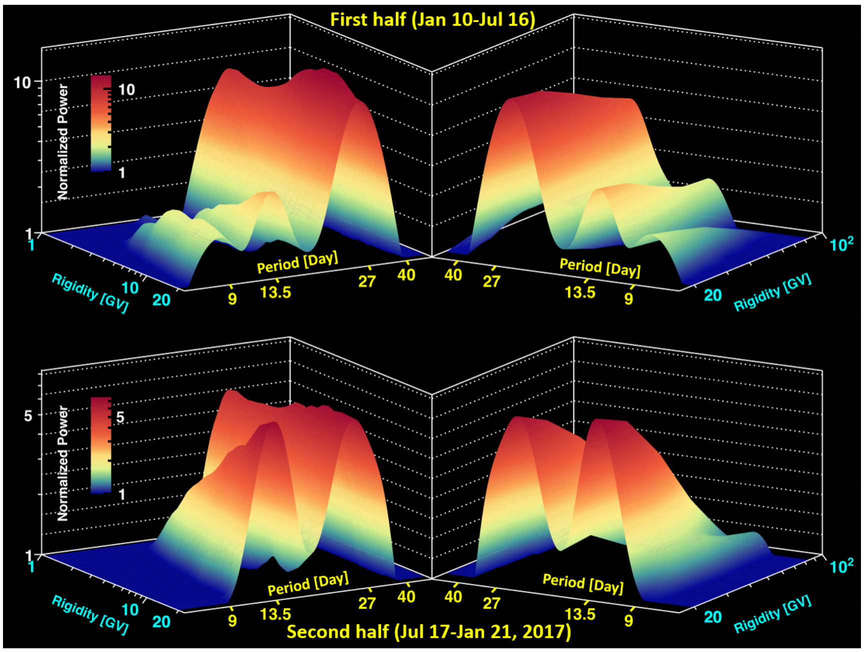

Figure 3: The normalized power as a function of rigidity and period for the first (top) and the second half (bottom) of 2016 from 1 to 20 GV (left) and from 20 GV to 100 GV (right).

4. Properties of Daily Helium Fluxes

We present the daily time evolution of the helium flux from 1.71 to 100 GV. The measurement is based on 8.9×10^8 helium nuclei collected by AMS during the first 10.5 years of operation. This is an update of the published AMS daily helium fluxes based on the first 8.5 years of operation in [22]. See also [28] for more details.

Fig. 4(a) shows the daily AMS helium fluxes, $\Phi_{\rm He}$, for six rigidity bins from 1.71 to 10.10 GV measured from May 20, 2011 to November 2, 2021. As seen, the daily helium flux exhibits variations on different timescales, from days to years. The relative magnitude of these variations decreases with increasing rigidity. At low rigidities, recurrent flux variations are clearly visible.

To study the recurrent time variations in the daily helium fluxes, a wavelet time-frequency technique [29] was used to locate the time intervals where the periodic structures emerge. Similar periodic structures as shown in the previous section for the daily proton fluxes also have been observed in the daily helium fluxes.

Fig. 4(b) shows Φ_{He}, Φ_p, and (c) $\Phi_{\mathrm{He}}/\Phi_p$ as a function of time for the rigidity bin [1.71-1.92] GV. As seen, $\Phi_{\mathrm{He}}/\Phi_p$ exhibits variations on multiple timescales. On short scales, $\Phi_{\mathrm{He}}/\Phi_p$ has a dip lasting months corresponding to the dip observed in Φ_{He}. On long timescales, the $\Phi_{\mathrm{He}}/\Phi_p$ reaches a minimum in 2013-2014, when the Φ_{He} is also in its minimum, and a maximum in 2018-2019, when the Φ_{He} is also in its maximum.

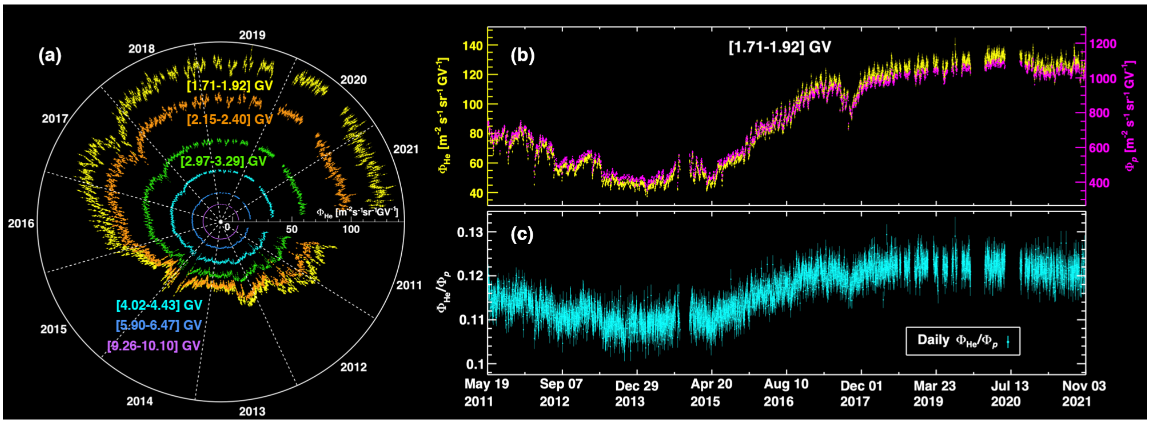

Figure 4: (a) The daily AMS helium fluxes, Φ_{He}, in units of [m^{-2}sr^{-1}s^{-1}GV^{-1}] for six rigidity bins from 1.71 to 10.10 GV measured from May 20, 2011 to November 2, 2021 (b) Φ_{He} (yellow) and Φ_p (magenta) and (c) $\Phi_{\mathrm{He}}/\Phi_p$ (cyan) measured from May 20, 2011 to November 2, 2021 at [1.71 – 1.92] GV.

We study the variation on the flux ratio $\Phi_{\mathrm{He}}/\Phi_p$ averaged over the period (2018-2019) and ratio $\Phi_{\mathrm{He}}/\Phi_p$ averaged over the period (2013-2014) as a function of rigidity. As shown in Fig. 5(a), $\Phi_{\mathrm{He}}/\Phi_p(2018\text{-}2019) > \Phi_{\mathrm{He}}/\Phi_p(2013\text{-}2014)$ for rigidities below ~ 7 GV. This implies that $\Phi_{\mathrm{He}}(2018\text{-}2019)/\Phi_{\mathrm{He}}(2013\text{-}2014) > \Phi_p(2018\text{-}2019)/\Phi_p(2013\text{-}2014)$; i.e., Φ_{He} exhibits larger time variations than Φ_p at low rigidities. As seen in figure 5(a), $\Phi_{\mathrm{He}}/\Phi_p$ is time independent above ~ 7 GV.

To investigate the difference of modulation in helium fluxes and proton fluxes, we consider in more detail the daily $\Phi_{\mathrm{He}}/\Phi_p$ as a function of daily Φ_{He}. Fig. 5(b) shows $\Phi_{\mathrm{He}}/\Phi_p$ as a function of daily Φ_{He} both calculated with the moving average of 14 BRs with a step of one day for the rigidity bin [1.71-1.92] GV. Different colors indicate different years from 2011 to 2021. As seen in Fig. 5(b), a hysteresis between $\Phi_{\mathrm{He}}/\Phi_p$ and Φ_{He} is observed before and after the solar maximum in 2014. To assess the significance of this hysteresis, we study the difference (in units of σ) of $\Phi_{\mathrm{He}}/\Phi_p$ at the same Φ_{He} but different solar conditions. We select the two time intervals with the same Φ_{He}, one before 2014 and one after, with the most significant difference in $\Phi_{\mathrm{He}}/\Phi_p$. To obtain the overall significance of the hysteresis, we repeat the procedure for remaining non-overlapping time intervals. The analysis is repeated for other rigidity bins. The hysteresis is observed at greater than the 7σ level below 2.4 GV. This shows that at low rigidity the modulation of $\Phi_{\mathrm{He}}/\Phi_p$ is different before and after the solar maximum in 2014.

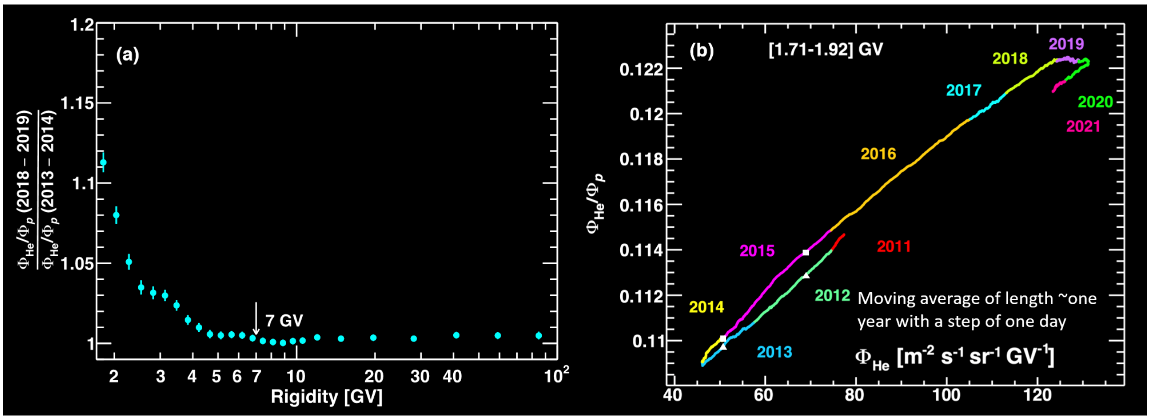

Figure 5: (a) The ratio of $\Phi_{\mathrm{He}}/\Phi_p$(2018-2019) and $\Phi_{\mathrm{He}}/\Phi_p$(2013-2014) as a function of rigidity. (b) $\Phi_{\mathrm{He}}/\Phi_p$ as a function of Φ_{He} both calculated with a moving average of length 14 BRs with a step of one day for the rigidity bin [1.71-1.92] GV. Different colors indicate different years from 2011 to 2021.

5. Temporal Structures in Electron Spectra and Charge Sign Effects in Galactic Cosmic Rays

We present the precision measurements of daily cosmic electron fluxes in the rigidity interval from 1.00 to 41.9 GV based on 2.0×10^8 electrons collected by AMS during the first 10.5 years of operation [23].

Fig. 6 shows the daily electron fluxes, Φ_{e^-}, and the daily proton fluxes, Φ_p, for four rigidity bins from 1.00 to 11.0 GV measured from May 20, 2011 to November 2, 2021. As seen, Φ_{e^-} exhibits both short-term variations on the scale of days to months and long-term variations on the scale of years, and the relative magnitude of these variations decreases with increasing rigidity. The time-dependent behavior of the Φ_{e^-} and Φ_p is distinctly different, and the differences decrease with increasing rigidity. From 2011 to 2014, Φ_{e^-} decreases faster with time than Φ_p. From 2015 to mid-2017, Φ_{e^-} increase more slowly than Φ_p below about 4 GV [Figs. 6(a) and 6(b)]. From mid-2020 to 2021, Φ_{e^-} decreases faster than Φ_p.

The comparison of the nonrecurrent variation of daily Φ_{e^-} and Φ_p for three short time intervals is shown in Fig. 7. As seen, during lower solar activity (left and right columns of Fig. 7), a difference between the short-term evolution of electrons and protons is observed, while during the solar maximum (middle column of Fig. 7), the difference vanishes. For instance, in Figs. 7(b) and 7(j), the slope of the recovery after the dip is different between electrons and protons. These observations indicate a charge-sign dependence in nonrecurrent solar modulation.

To study the recurrent variations in Φ_{e^-}, a wavelet time-frequency technique [29] was used to locate the time intervals where the periodic structures emerge. Fig. 8 shows the normalized power as a function of rigidity and period for Φ_{e^-} and Φ_p during two time intervals when the 27-day periodicity is most prominent (second half of 2011 and first half of 2017). As seen, the rigidity dependence behavior of the normalized power of electrons and protons is different in these two time intervals. In particular, in the second half of 2011 [Figs. 8(a) and 8(b)], the strength of the 27-day period of electrons is greater than that of protons, while in the first half of 2017 [Figs. 8(c) and 8(d)], the strength of the 27-day period of electrons is less than that of protons.

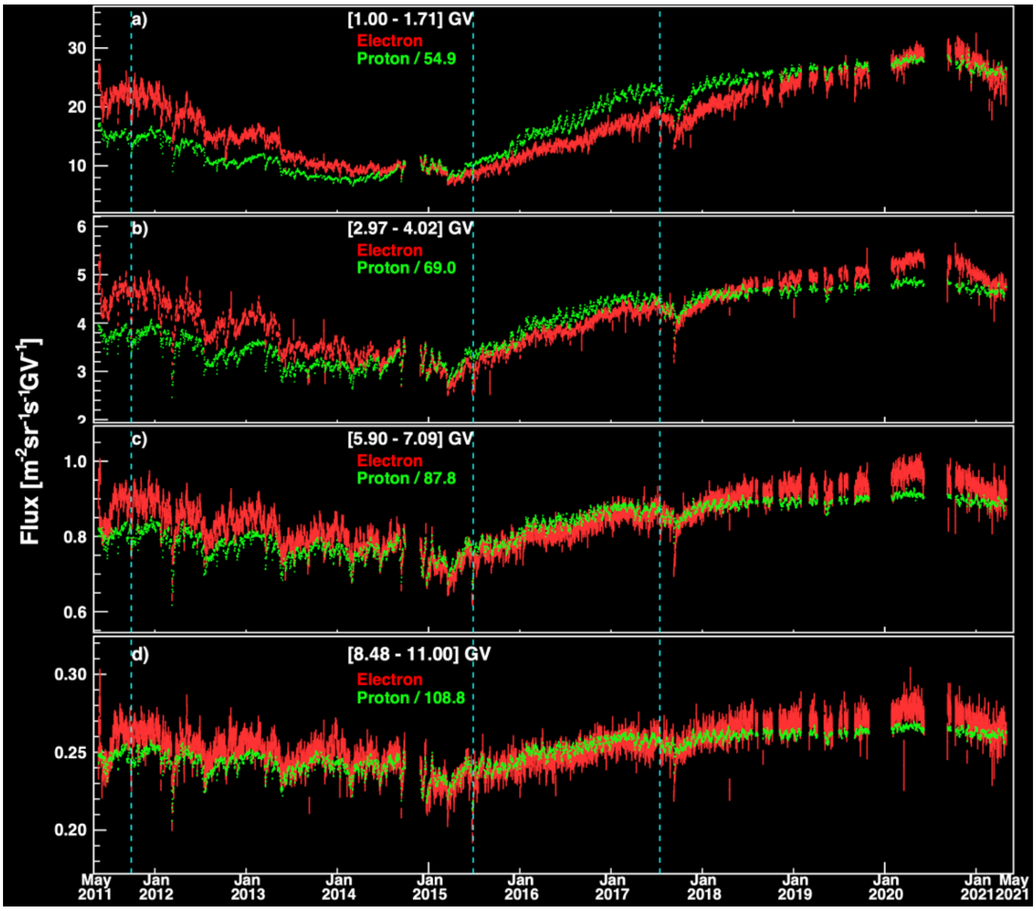

Figure 6: Daily electron fluxes, Φ_{e^-}, and daily proton fluxes, Φ_p, in units of [m^{-2}sr^{-1}s^{-1}GV^{-1}] for four rigidity bins from 1.00 to 11.0 GV measured from May 20, 2011 to November 2, 2021.

Fig. 9(a,b) shows Φ_{e^-} as a function of Φ_p for the [1.00-1.71] GV. For Fig. 9(a), the data points are the daily AMS measurements of Φ_{e^-} and Φ_p. For Fig. 9(b), both Φ_{e^-} and Φ_p are calculated with a moving average of 14 BRs with a step of 1 day. Different colors indicate different years from 2011 to 2021. As seen, a hysteresis between Φ_{e^-} and Φ_p is observed; that is, from 2011 to 2018 at a given electron flux, the proton flux shows two distinct branches with time, one before 2014–2015 and one after. Both electron and proton fluxes peak in 2020, after which the hysteresis curve starts to trace the earlier behavior (2018–2020) backwards. This is consistent with the differences in electron and proton modulation being symmetric with respect to the minimum solar modulation.

To assess the significance of this hysteresis we study, at different solar conditions, the values of Φ_p at the same Φ_{e^-}. We select the two time intervals with the same Φ_{e^-}, one before 2014-2015 and one after, with the most significant difference in Φ_p (A, B). We repeat the procedure for remaining non-overlapping time intervals (C, D). Figure 9(c) shows the proton flux ratios Φ_p^B/Φ_p^A and Φ_p^D/Φ_p^C as a function of rigidity. As seen, the difference in Φ_p decreases with increasing rigidity and the hysteresis is observed with a significance greater than 6σ below 8.48 GV.

To probe structures in the hysteresis, the moving averages of the Φ_{e^-} and Φ_p are calculated with a finer time window. The results for the rigidity interval of [1.00–1.71] GV are shown in Fig.

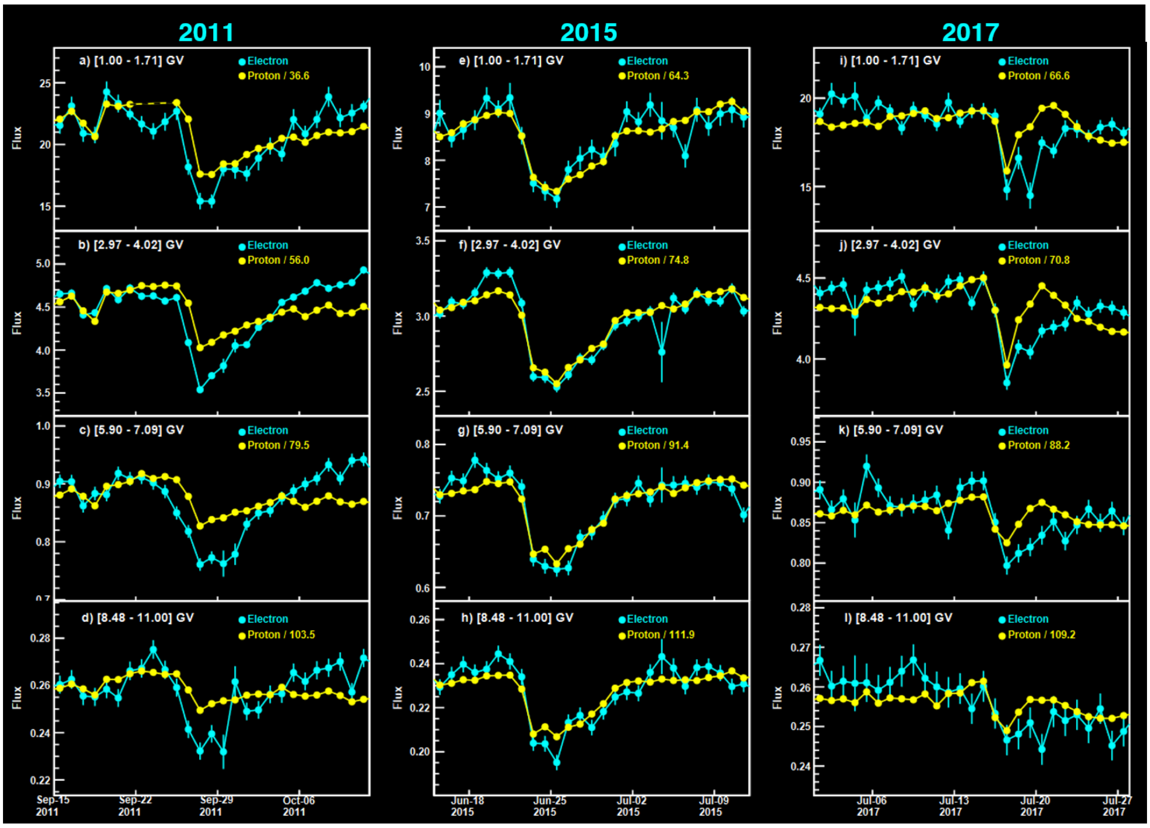

Figure 7: Daily electron fluxes, Φ_{e^-}, (red points) and proton fluxes, Φ_p, (blue points) in units of $[\mathrm{m^{-2}sr^{-1}s^{-1}GV^{-1}}]$ during three time intervals: (a, b, c, d) from September 15 to October 12, 2011, (e, f, g, h) from June 15 to July 12, 2015, (i, j, k, l) from July 1 to July 28, 2017, for four rigidity bins from 1.00 to 11.0 GV in each case.

10. Figure 10(a) shows the daily Φ_{e^-} and Φ_p as a function of time for the 11-year period. The arrows I, II, and III indicate the location of sharp dips in the proton and electron fluxes, and the colored bands IV and V mark the time intervals around the dips in 2015 and 2017. The moving average of Φ_{e^-} and Φ_p with the time window of 2 BRs and a step of 1 day for this rigidity interval is shown in Fig. 10(b). The detailed behavior around the dips IV and V is shown in Fig. 10(c,d). To assess the significance of these structures in hysteresis, we study the difference of Φ_{e^-} at the same Φ_p, one in the first half and one in the second half of each region. The significance of the hysteresis structure at [1.00–1.71] GV corresponding to the large dip in 2015 is 15.9σ (IV) and to the large dip in 2017 is 7.0σ (V).

The structures in the hysteresis in 2015 and 2017 are likely caused by a series of interplanetary coronal mass ejections [30]. The clear deviation from the long-term trend implies a charge-sign-dependent modulation during those solar transients on the timescale of several Bartels rotations.

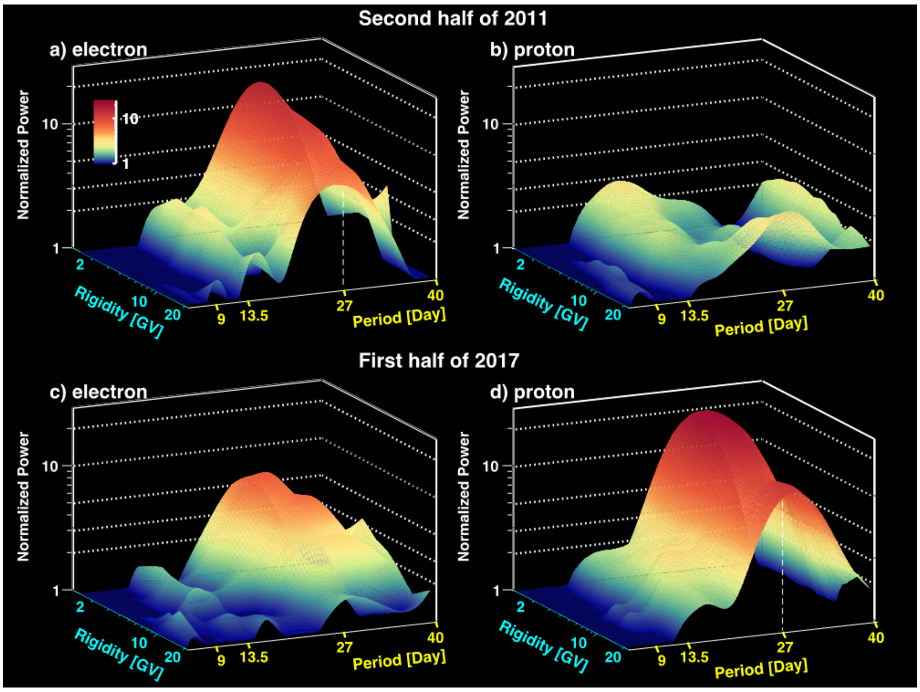

Figure 8: Normalized power of (a,c) electron fluxes and (b,d) proton fluxes as a function of rigidity and time for (a,b) the second half of 2011 (May 20 to December 16, 2011) and (c,d) the first half of 2017 (January 22 to July 2, 2017).

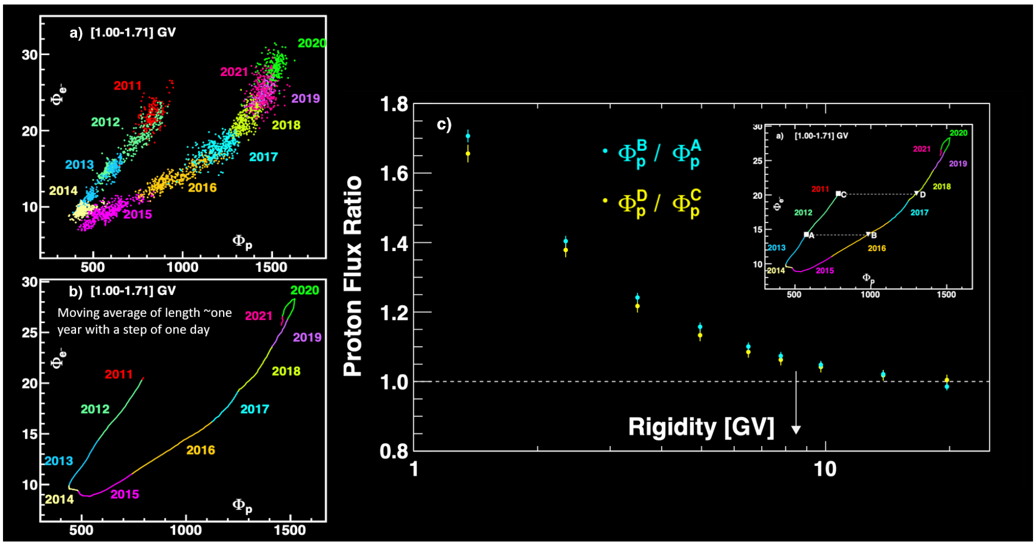

Figure 9: (a,b) Electron fluxes, Φ_{e^-}, versus the proton fluxes, Φ_p, in units of [m^{-2}sr^{-1}s^{-1}GV^{-1}] for the rigidity bin [1.00-1.71] GV. For (a), the data points are the daily Φ_{e^-} and Φ_p. For (b), both Φ_{e^-} and Φ_p are calculated with a moving average of 14 BRs with a step of 1 day. Different colors indicate different years from 2011 to 2021. (c) The proton flux ratios Φ_p^B/Φ_p^A (cyan data points) and Φ_p^D/Φ_p^C (yellow data points) at two Φ_{e^-} as a function of rigidity from 1.00 to 22.8 GV. The insert in (c) shows an example of the two pair of points, (A, B) and (C, D), at two Φ_{e^-} used to calculate the significance of the hysteresis.

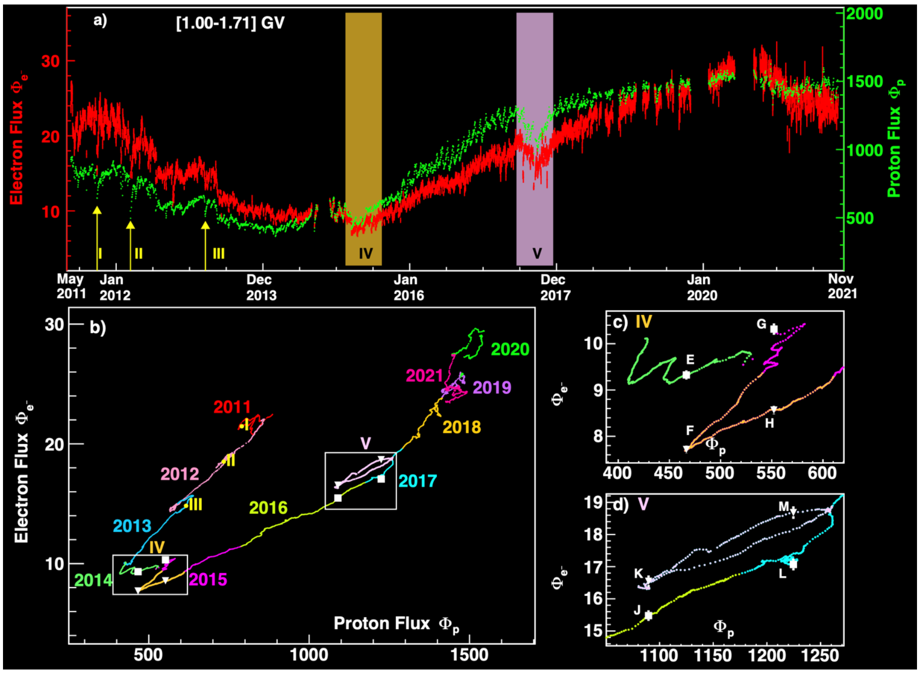

Figure 10: (a) The daily electron fluxes, Φ_{e^-}, (red, left axis) and daily proton fluxes, Φ_p, (green, right axis) in units of $[\mathrm{m}^{-2}\mathrm{sr}^{-1}\mathrm{s}^{-1}\mathrm{GV}^{-1}]$ as a function of time for the rigidity interval of 1.00 to 1.71 GV. The arrows I, II, and III indicate the location of sharp dips in the proton and electron fluxes, and the colored bands IV and V mark the time intervals around the dips in 2015 and 2017. (b) Φ_{e^-} versus Φ_p both calculated with a moving average of 2 BRs and a step of 1 day. The location of I, II, and III correspond to the flux dips in (a). The dips in 2015 (IV) and 2017 (V) are indicated by white boxes.

6. Temporal Structures in Positron Spectra and Charge Sign Effects in Galactic Cosmic Rays

We present the precision measurements of daily cosmic positron fluxes in the rigidity range from 1.00 to 41.9 GV based on 3.4×10^6 positrons collected by AMS during the first 10.5 years of operation [31].

Fig. 11 shows the daily positron flux, Φ_{e^+}, in the rigidity range from 1.00 to 1.71 GV, measured from May 20, 2011 to November 2, 2021, together with (a) the daily electron flux, Φ_{e^-}, and (b) the daily proton flux, Φ_p, both measured by AMS in the same rigidity range and time period. As seen, Φ_{e^+} exhibits short-term variations on the scale of days to months, and long-term variations on the scale of years. Fig. 11(a) shows that the long-term evolution of positron and electron fluxes is clearly different. On the contrary, Fig. 11(b) shows that positron and proton fluxes present a similar behavior over time.

To investigate the difference in the modulation of Φ_{e^+} , Φ_{e^-} and Φ_p, Fig. 12 shows Φ_{e^-} and Φ_p as functions of Φ_{e^+} in the rigidity range from 1.00 to 1.71 GV. For Fig. 12(a,b) the data points correspond to fluxes averaged over 3 days. For Fig. 12(c,d), Φ_{e^+} , Φ_{e^-} and Φ_p are calculated with a moving average of 14 BRs and a step of 3 days. Different colors indicate different years from 2011 to 2021. In Fig. 12(c) a hysteresis between Φ_{e^+} and Φ_{e^-} is clearly observed. From 2011 to 2018 at a given Φ_{e^-} , Φ_{e^+} shows two distinct branches with time, one before 2014–2015 and one

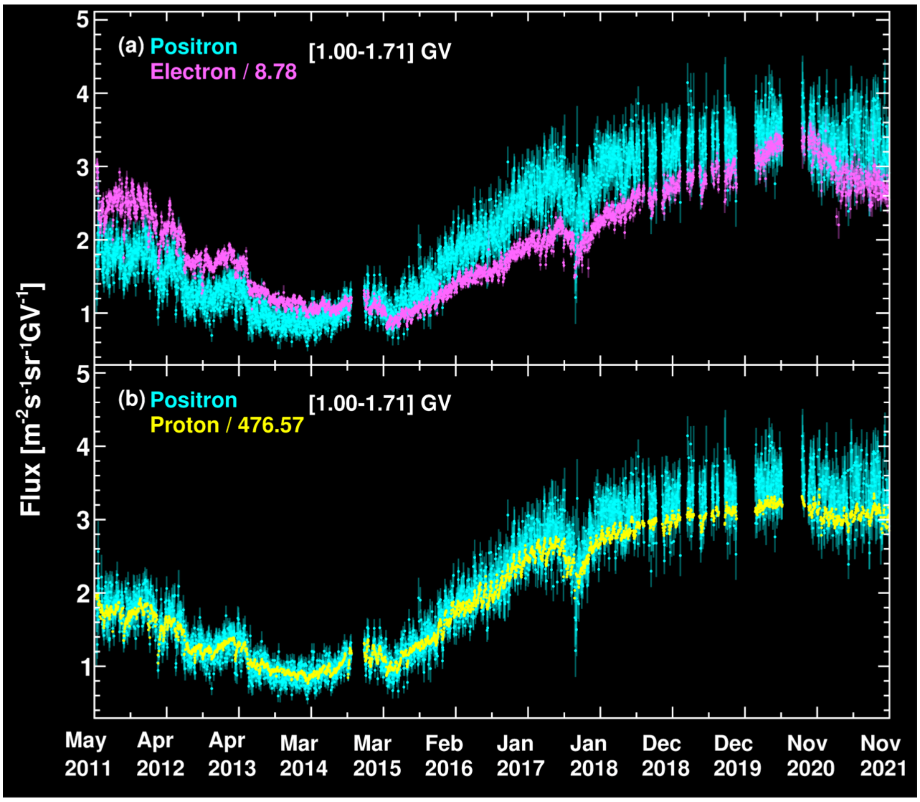

Figure 11: The daily positron fluxes, Φ_{e^+}, (light blue points) measured over the entire period for the rigidity range from 1.00 to 1.71 GV together with (a) the daily electron fluxes, Φ_{e^-}, (magenta points), and (b) the daily proton fluxes, Φ_p, (yellow points). Fluxes are in units of $[\mathrm{m^{-2}sr^{-1}s^{-1}GV^{-1}}]$.

after. Around 2017 the hysteresis curve changes such that in 2018–2020 it is nearly parallel to that in 2011–2013. Similar behavior is observed in the Φ_{e^-} to Φ_p correlation. On the contrary, as seen from Fig. 12(d), there is a nearly linear correlation between Φ_{e^+} and Φ_p in the entire time period. Fig. 12 also shows that the three fluxes, Φ_{e^+} , Φ_{e^-} and Φ_p peak in 2020 after which the fluxes start to trace their earlier behavior (2018-2020) backwards.

To compare the daily time variations of Φ_{e^+} and Φ_p, we fit a linear relation between the relative variations of the fluxes for the ith rigidity bin, $(R_i, R_i + \Delta R_i)$, as:

$$\frac{\Phi^i_{e^+} - < \Phi^i_{e^+} >}{< \Phi^i_{e^+} >} = k^i \cdot \frac{\Phi^i_p - < \Phi^i_p >}{< \Phi^i_p >} \tag{1}$$

where k^i is the slope of the linear dependence for that bin and $< \Phi^i_{e^+} >$ and $< \Phi^i_p >$ are the positron and proton fluxes in the ith rigidity bin averaged over the entire period, respectively. Fig. 13(a) shows an example of the linear fit of the daily positron and the daily proton fluxes to Eq. 1 for the rigidity bin [1.00-1.33] GV. Fig. 13(b) shows the results of the k^i as a function of rigidity. As shown in Fig. 13(b), k^i is greater than unity with a significance greater than 5σ for rigidities from 1.00 GV to 7.09 GV indicating that the positron flux is more modulated than the proton flux in this rigidity range.

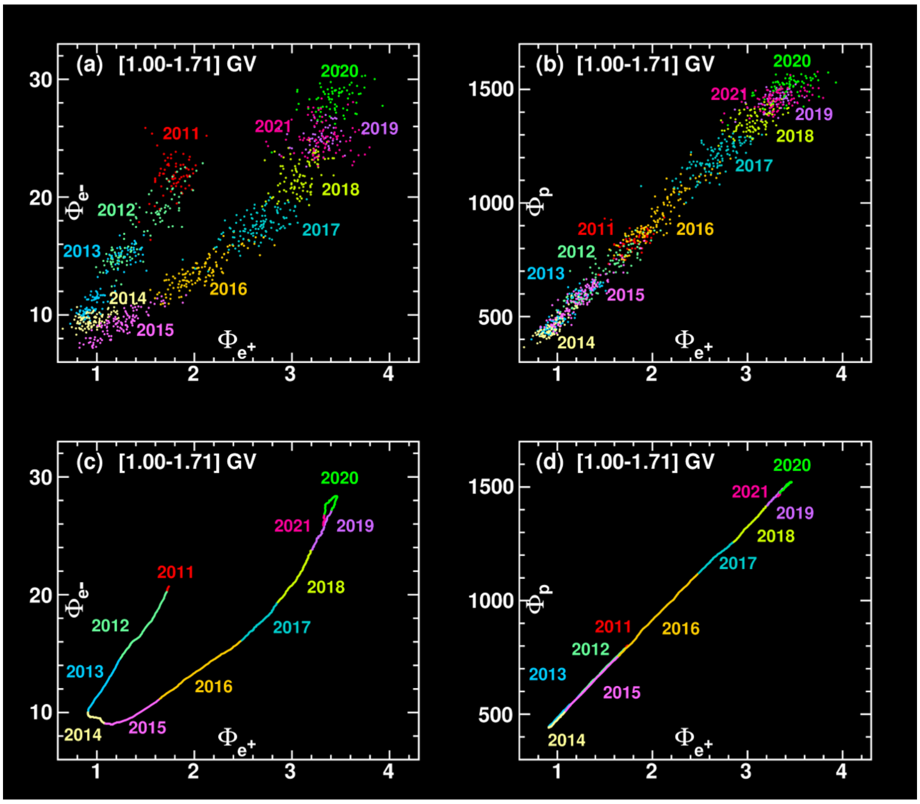

Figure 12: In the rigidity range from 1.00 to 1.71 GV, (a,c) electron flux, Φ_{e^-}, versus positron flux, Φ_{e^+}, and (b,d) proton flux, Φ_p, versus positron flux, Φ_{e^+}. For (a,b) the data points correspond to fluxes averaged over 3 days. For (c,d), Φ_{e^-}, Φ_p and Φ_{e^+} , are calculated with a moving average of 14 BRs and a step of 3 days. Fluxes are in units of [$\mathrm{m^{-2}sr^{-1}s^{-1}GV^{-1}}$]. Different colors indicate different years.

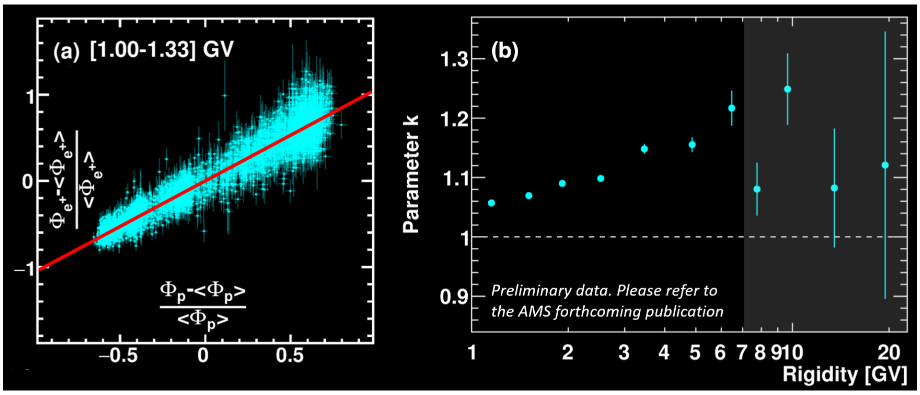

Preliminary data. Please refer to the AMS forthcoming publication

Figure 13: (a) The relative variation of the daily Φ_{e^+} , $\frac{\Phi_{e^+}-<\Phi_{e^+}>}{<\Phi_{e^+}>}$, versus the relative variation of the daily Φ_p, $\frac{\Phi_p-<\Phi_p>}{<\Phi_p>}$, for the rigidity interval [1.00-1.33] GV. The solid red line is the result of the fit of Eq. 1 to the data. (b) k parameter values obtained from the linear fits to the relative variation of the positron and proton daily fluxes as function of rigidity.

7. Conclusions

The latest time variation measurements by AMS cover the major portion of solar cycle 24, which includes the polarity reversal of the solar magnetic field in the year 2013, and the beginning of solar cycle 25. These continuous daily data provide unique and precise input to the understanding of the charge sign and mass dependencies of cosmic rays over an 11-year solar cycle. During the lifetime of the mission in space, AMS will also cover the solar cycle 25 and, in particular, the next solar magnetic field polarity reversal. This extensive set of continuous precision measurements of elementary particles and nuclei performed by a single detector over a long time period pave the way to develop a comprehensive understanding of the cosmic ray transport in the heliosphere.

References

[1] A. W. Strong and I. V. Moskalenko, Propagation of cosmic-ray nucleons in the galaxy, Astrophys. J. **509**, 212 (1998); A. E. Vladimirov, S. W. Digel, G. Jóhannesson, P. F. Michelson, I. V. Moskalenko, P. L. Nolan, E. Orlando, T. A. Porter, and A. W. Strong, GALPROP WebRun: An internet-based service for calculating galactic cosmic ray propagation and associated photon emissions, Comput. Phys. Commun. **182**, 1156 (2011).

[2] C. Evoli, D. Gaggero, A. Vittino, G. Di Bernardo, M. Di Mauro, A. Ligorini, P. Ullio, and D. Grasso, Cosmic-ray propagation with DRAGON2: I. Numerical solver and astrophysical ingredients, J. Cosmol. Astropart. Phys. 02 (2017) 015.

[3] D. Maurin, F. Donato, R. Taillet, and P. Salati, Cosmic rays below $Z = 30$ in a diffusion model: New constraints on propagation parameters, Astrophys. J. **555**, 585 (2001).

[4] A. Putze, L. Derome, and D. Maurin, A Markov chain Monte Carlo technique to sample transport and source parameters of galactic cosmic rays II. Results for the diffusion model combining B/C and radioactive nuclei, Astron. Astrophys. **516**, A66 (2010).

[5] M. S. Potgieter, Solar modulation of cosmic rays, Living Rev. Solar Phys. **10**, 3 (2013).

[6] E. N. Parker, The passage of energetic charged particles through interplanetary space, Planet. Space Sci. **13**, 9 (1965).

[7] D. H. Hathaway, The solar cycle, Living Rev. Solar Phys. **12**, 4 (2015).

[8] Sunspot data from the World Data Center SILSO, Royal Observatory of Belgium, Brussels at http://www.sidc.be/silso/cyclesminmax.

[9] M. Zhang, Modulation of galactic cosmic rays at solar maximum: Observations, Adv. Space Res. **32**, 603 (2003); H. V. Cane, Coronal mass ejections and Forbush decreases, Space Sci. Rev. **93**, 55 (2000); M. S. Potgieter, J. A. Le Roux, L. F. Burlaga, and F. B. McDonald, The role of merged interaction regions and drifts in the heliospheric modulation of cosmic rays beyond 20 AU: A computer simulation, Astrophys. J. **403**, 760 (1993); G. Wibberenz, I. G. Richardson, and H. V. Cane, A simple concept for modeling cosmic ray modulation in the inner heliosphere during solar cycles 2023, J. Geophys. Res. **107**, 1353 (2002).

[10] J. A. Simpson, A brief history of recurrent solar modulation of the galactic cosmic rays (1937-1990), Space Sci. Rev. **83**, 169 (1998).

[11] C. Paizis *et al.*, Amplitude evolution and rigidity dependence of the 26-day recurrent cosmic ray decreases: COSPIN/KET results, J. Geophys. Res. **104**, 28241 (1999).

[12] Z. Shen, G. Qin, P. Zuo, F. Wei, and X. Xu, A study of variations of galactic cosmic-ray intensity based on a hybrid data-processing method, Astrophys. J. 900, 143 (2020).

[13] R. Modzelewska *et al.*, Study of the 27 day variations in GCR fluxes during 2007–2008 based on PAMELA and ARINA observations, Astrophys. J. **904**, 3 (2020), In this paper, the rigidity dependence of the 27-day periodicity in 2007-2008 has been directly measured.

[14] R. Modzelewska and A. Gil, Recurrence of galactic cosmic-ray intensity and anisotropy in solar minima 23/24 and 24/25 observed by ACE/CRIS, STEREO, SOHO/EPHIN and neutron monitors, Astron. Astrophys. **646**, A128 (2021).

[15] A. López-Comazzi and J. J. Blanco, Short-term periodicities observed in neutron monitor counting rates, Sol. Phys. **295**, 81 (2020).

[16] M. Armano *et al.*, Characteristics and energy dependence of recurrent galactic cosmic-ray flux depressions and of a Forbush decrease with LISA pathfinder, Astrophys. J. **854**, 113 (2018).

[17] I. Sabbah and K. Kudela, Third harmonic of the 27 day periodicity of galactic cosmic rays: Coupling with interplanetary parameters, J. Geophys. Res. **116**, A04103 (2011).

[18] M. Temmer, B. Vršnak, and A. M. Veronig, Periodic appearance of coronal holes and the related variation of solar wind parameters, Sol. Phys. **241**, 371 (2007).

[19] S. E. Forbush, On cosmic-ray effects associated with magnetic storms, Terr. Magn. Atmos. Electr. **43**, 203 (1938).

[20] A. Gil and M. V. Alania, Theoretical and experimental studies of the rigidity spectrum of the 27-day variation of the galactic cosmic ray intensity in different epochs of solar activity, Sol. Phys. **283**, 565 (2013).

[21] M. Aguilar *et al.* (AMS Collaboration), Periodicities in the Daily Proton Fluxes from 2011 to 2019 Measured by the Alpha Magnetic Spectrometer on the International Space Station from 1 to 100 GV, Phys. Rev. Lett. **127**, 271102 (2021).

[22] M. Aguilar *et al.* (AMS Collaboration), Properties of Daily Helium Fluxes, Phys. Rev. Lett. **128**, 231102 (2022).

[23] M. Aguilar *et al.* (AMS Collaboration), Temporal Structures in Electron Spectra and Charge Sign Effects in Galactic Cosmic Rays, Phys. Rev. Lett. **130**, 161001 (2023).

[24] M. S. Potgieter, The charge-sign dependent effect in the solar modulation of cosmic rays, Adv. Space Res. **53**, 1415 (2014).

[25] C. Corti, M. S. Potgieter, V. Bindi, C. Consolandi, C. Light, M. Palermo, and A. Popkow, Numerical modeling of galactic cosmic-ray proton and helium observed by AMS-02 during the solar maximum of Solar Cycle 24, Astrophys. J. **871**, 253 (2019); N. Tomassetti, F. Barão, B. Bertucci, E. Fiandrini, and M. Orcinha, Numerical modeling of cosmic-ray transport in the heliosphere and interpretation of the proton-to-helium ratio in Solar Cycle 24, Adv. Space Res. **64**, 2477 (2019); M. D. Ngobeni, O. P. M. Aslam, D. Bisschoff, M. S. Potgieter, D. C. Ndiitwani, M. Boezio, N. Marcelli, R. Munini, V. V. Mikhailov, and S. A. Koldobskiy, The 3D numerical modeling of the solar modulation of galactic protons and helium nuclei related to observations by PAMELA between 2006 and 2009, Astrophys. Space Sci. **365**, 182 (2020).

[26] M. Aguilar *et al.* (AMS Collaboration), The Alpha Magnetic Spectrometer (AMS) on the International Space Station: Part II - Results from the First Seven Years, Phys. Rep. **894** 1 (2021).

[27] X. Sun, J. T. Hoeksema, Y. Liu, and J. Zhao, On polar magnetic field reversal and surface flux transport during solar cycle 24, Astrophys. J. **798**, 114 (2015).

[28] Y. Jia, Precision Measurement of Daily Proton and Helium Fluxes by the Alpha Magnetic Spectrometer, Proceedings of the 38th International Cosmic Ray Conference (ICRC2023).

[29] C. Torrence and G. P. Compo, A Practical Guide to Wavelet Analysis, Bull. Am. Meteorol. Soc. **79**, 61 (1998).

[30] I. Richardson and H. Cane, Near-Earth interplanetary coronal mass ejections since January 1996, https://izw1.caltech.edu/ACE/ASC/DATA/level3/icmetable2.htm, specifically the events starting from March 16, 2015 and from July 16, 2017.

[31] M. Aguilar *et al.* (AMS Collaboration), Temporal Structures in Positron Spectra and Charge Sign Effects in Galactic Cosmic Rays, Accepted for publication in Physical Review Letters.